

Shifting hail hazard under global warming: supplementary information

Timothy H. Raupach^{1,2,3}, Raphael Portmann^{4,5}, Christian Siderius⁶,
and Steven C. Sherwood^{2,3}

1: Institute for Climate Risk and Response, The University of New South Wales (UNSW), Sydney, Australia

2: Climate Change Research Centre, UNSW Sydney, Sydney, Australia

3: ARC Centre of Excellence for Climate Extremes, UNSW Sydney, Sydney, Australia

4: Agroscope, Swiss Federal Office for Agriculture, Zurich, Switzerland

5: Planval, Bern, Switzerland

6: Uncharted Waters Research, Sydney, Australia

1 Supplementary tables and figures

Model	Institution	Experiment	Ensemble	Start	End	Res	Vert	Orog
CMCC-CM2-SR5	CMCC	historical	r1i1p1f1	1980	1999	100 km	30.0	
CMCC-CM2-SR5	CMCC	ssp585 (2C)	r1i1p1f1	2037	2056	100 km	30.0	
CMCC-CM2-SR5	CMCC	ssp585 (3C)	r1i1p1f1	2054	2073	100 km	30.0	
CMCC-ESM2	CMCC	historical	r1i1p1f1	1980	1999	100 km	30.0	
CMCC-ESM2	CMCC	ssp585 (2C)	r1i1p1f1	2041	2060	100 km	30.0	
CMCC-ESM2	CMCC	ssp585 (3C)	r1i1p1f1	2056	2075	100 km	30.0	
CNRM-CM6-1	CNRM-CERFACS	historical	r1i1p1f2	1980	1999	250 km	91.0	
CNRM-CM6-1	CNRM-CERFACS	ssp585 (2C)	r1i1p1f2	2042	2061	250 km	91.0	X
CNRM-CM6-1	CNRM-CERFACS	ssp585 (3C)	r1i1p1f2	2057	2076	250 km	91.0	X
EC-Earth3	EC-Earth-Consortium	historical	r1i1p1f1	1980	1999	100 km	91.0	
EC-Earth3	EC-Earth-Consortium	ssp585 (2C)	r1i1p1f1	2031	2050	100 km	91.0	
EC-Earth3	EC-Earth-Consortium	ssp585 (3C)	r1i1p1f1	2052	2071	100 km	91.0	
GISS-E2-1-G	NASA-GISS	historical	r1i1p1f2	1980	1999	250 km	40.0	X
GISS-E2-1-G	NASA-GISS	ssp585 (2C)	r1i1p1f2	2028	2047	250 km	40.0	X
GISS-E2-1-G	NASA-GISS	ssp585 (3C)	r1i1p1f2	2055	2074	250 km	40.0	X
MIROC6	MIROC	historical	r1i1p1f1	1980	1999	250 km	81.0	
MIROC6	MIROC	ssp585 (2C)	r1i1p1f1	2051	2070	250 km	81.0	
MIROC6	MIROC	ssp585 (3C)	r1i1p1f1	2072	2091	250 km	81.0	
MPI-ESM1-2-HR	MPI-M	historical	r1i1p1f1	1980	1999	100 km	95.0	
MPI-ESM1-2-HR	DKRZ	ssp585 (2C)	r1i1p1f1	2053	2072	100 km	95.0	
MPI-ESM1-2-HR	DKRZ	ssp585 (3C)	r1i1p1f1	2075	2094	100 km	95.0	
MRI-ESM2-0	MRI	historical	r1i1p1f1	1980	1999	100 km	80.0	
MRI-ESM2-0	MRI	ssp585 (2C)	r1i1p1f1	2038	2057	100 km	80.0	
MRI-ESM2-0	MRI	ssp585 (3C)	r1i1p1f1	2062	2081	100 km	80.0	

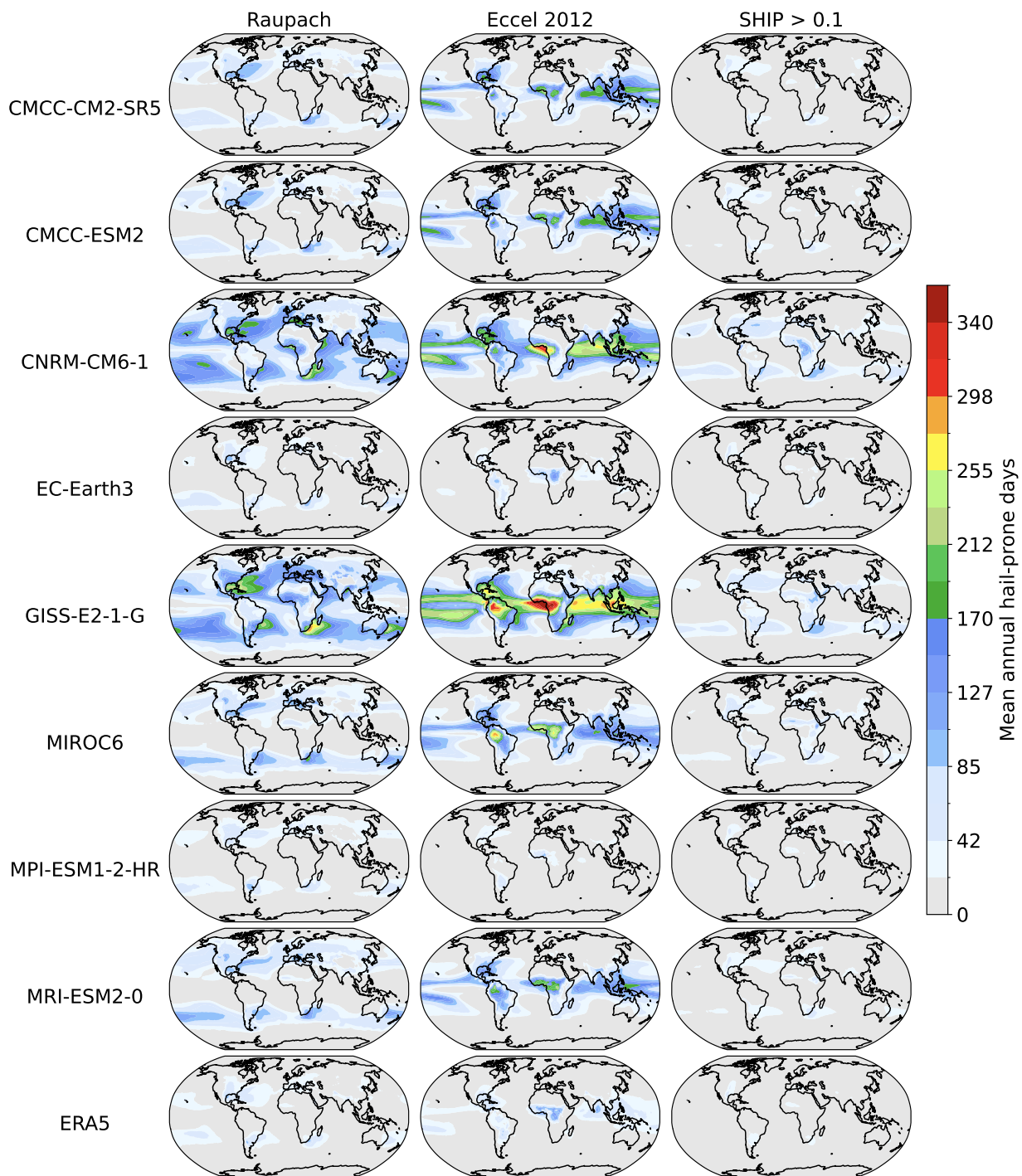
Table 1: **CMIP6 model details.** “Res” is nominal model resolution, “Vert” is the number of vertical levels in the model. An X in the column “Orog” indicates models for which no orography was provided; in these cases the orography for the historical run of CNRM-CM6-1 was interpolated to the model grid for use here.

2 Update to hail proxy

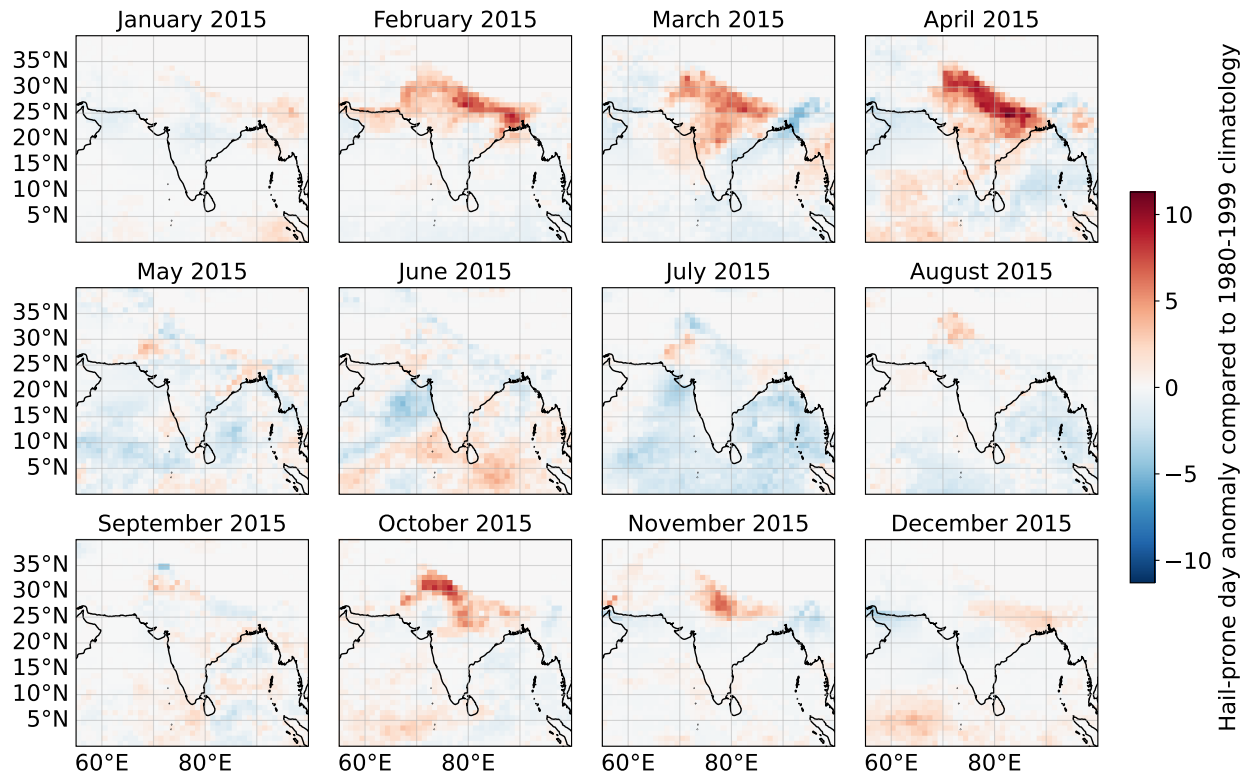
The instability-shear proxy of Raupach et al. [2023a] was slightly updated for this study, to be more globally applicable. This proxy indicates hail-prone conditions when

$$\text{CAPE} \times S_{06}^{\alpha} \geq \beta, \quad (1)$$

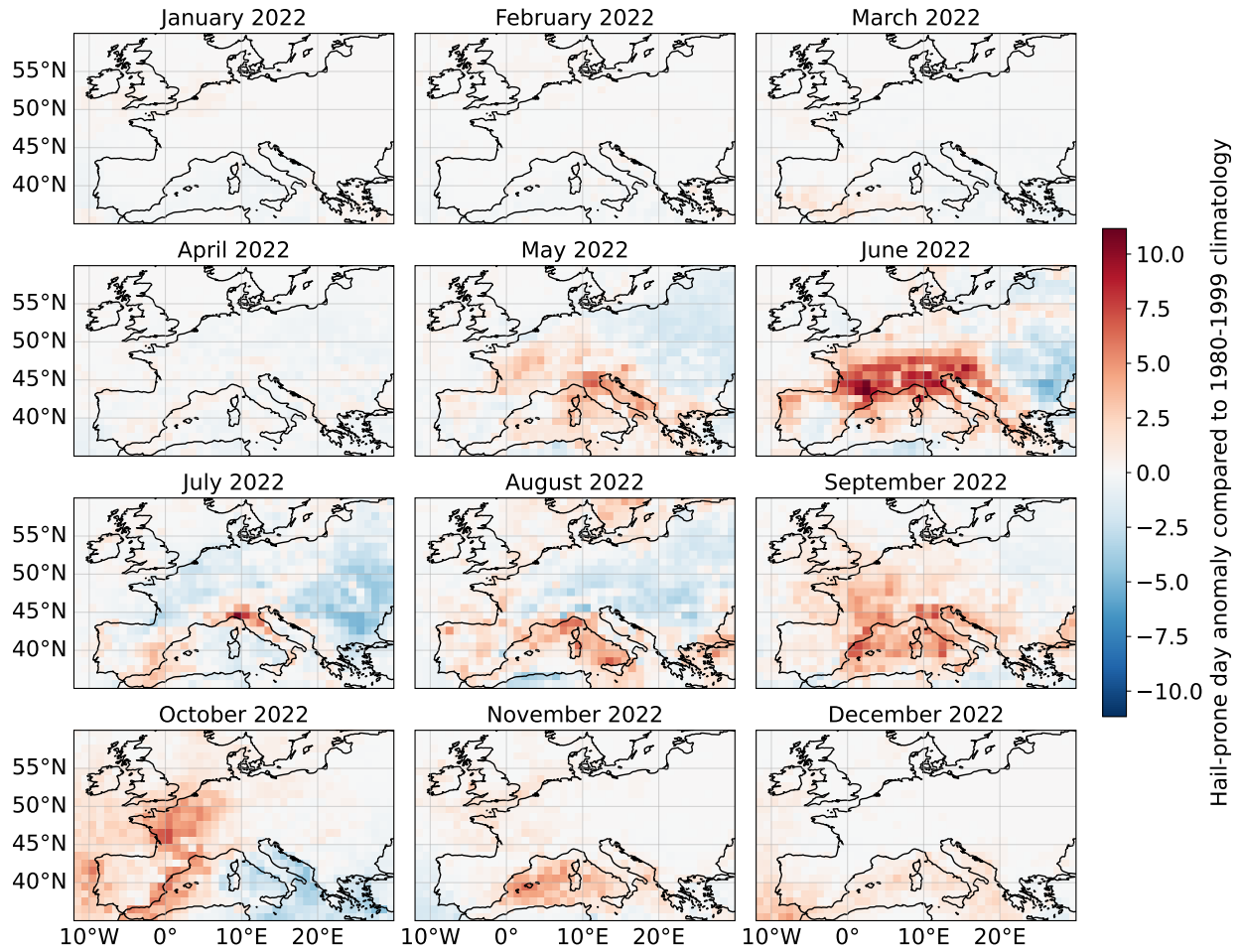
where CAPE is convective available potential energy, S_{06} is 0-6 km bulk vertical wind shear, and α and β are parameters that vary with the melting level height [Raupach et al., 2023a]. Figure 26 shows the Raupach et al. [2023a] proxy discriminator lines for various values of melting level height (MLH) above the surface. When the MLH is below about 1500 m, the value of α becomes



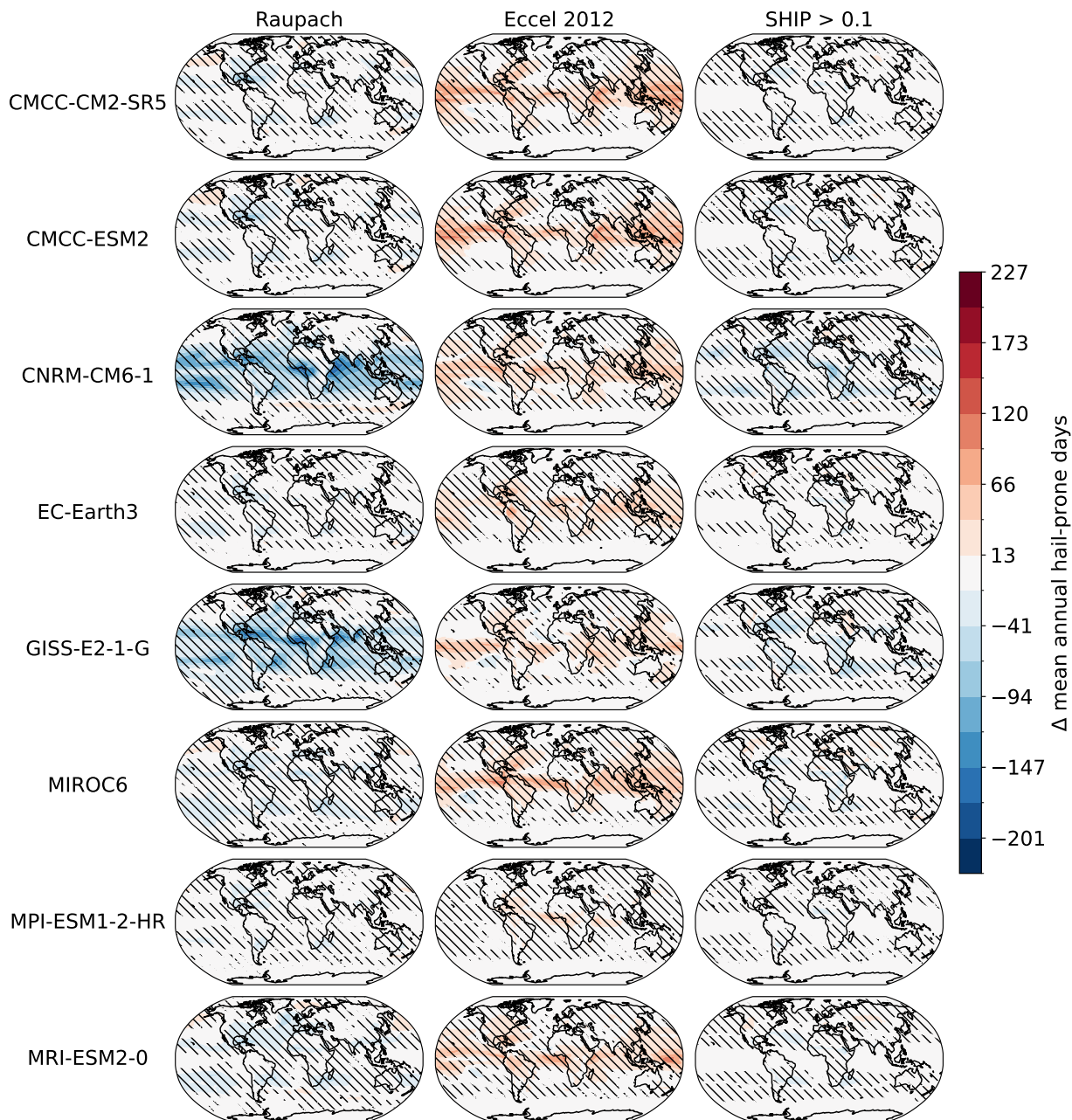
Supplementary Figure 1: **Mean annual hail-prone days in historical (1980-1999) runs.** Plots are by CMIP6 model and for ERA5 reanalysis data.



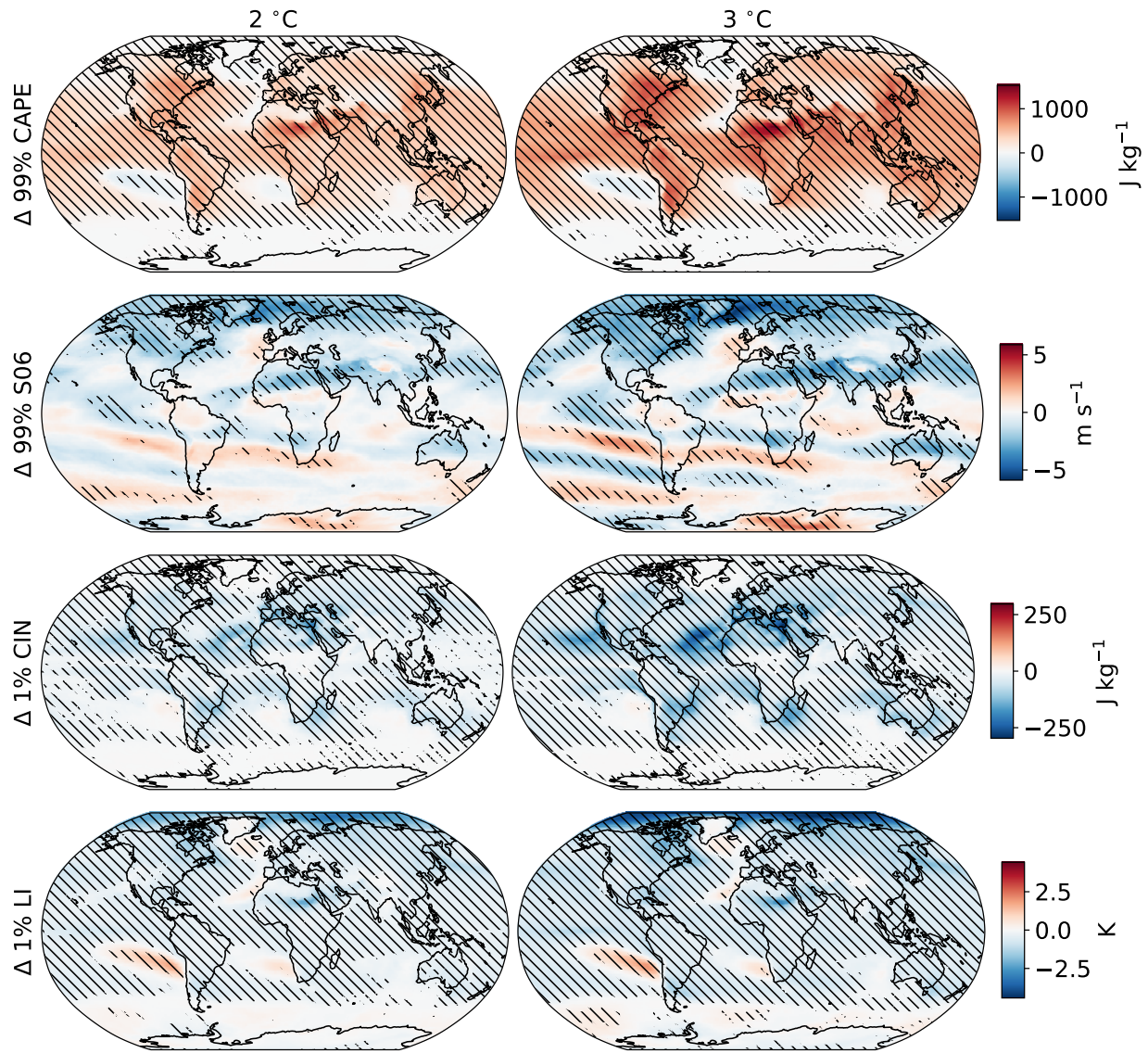
Supplementary Figure 2: Monthly multi-proxy mean hail-prone day anomalies for the Indian region in 2015. Anomalies are calculated using ERA5 data with respect to the monthly ERA5 historical climatology (1980-1999), figure shows multi-proxy mean anomalies.



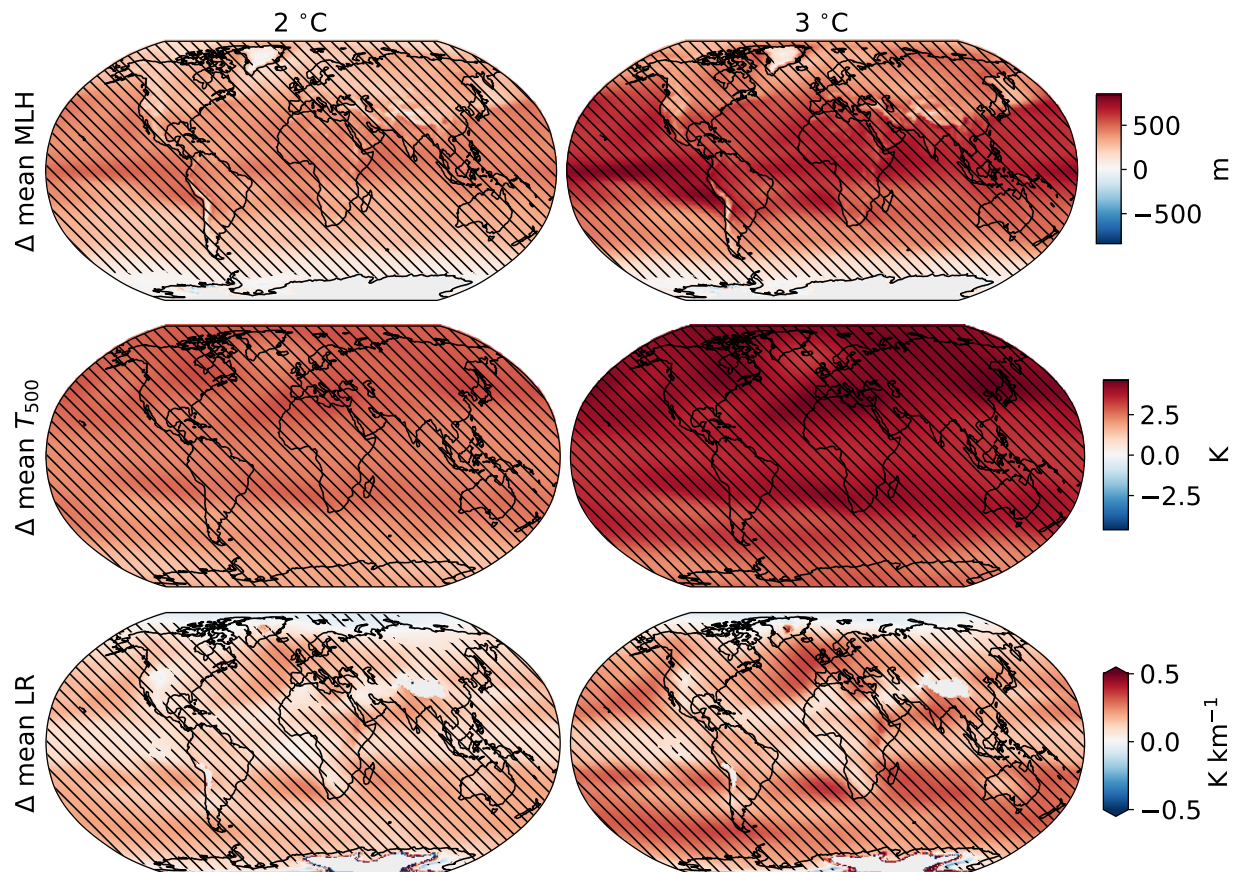
Supplementary Figure 3: As for Supplementary Figure 2 but for Europe in 2022.



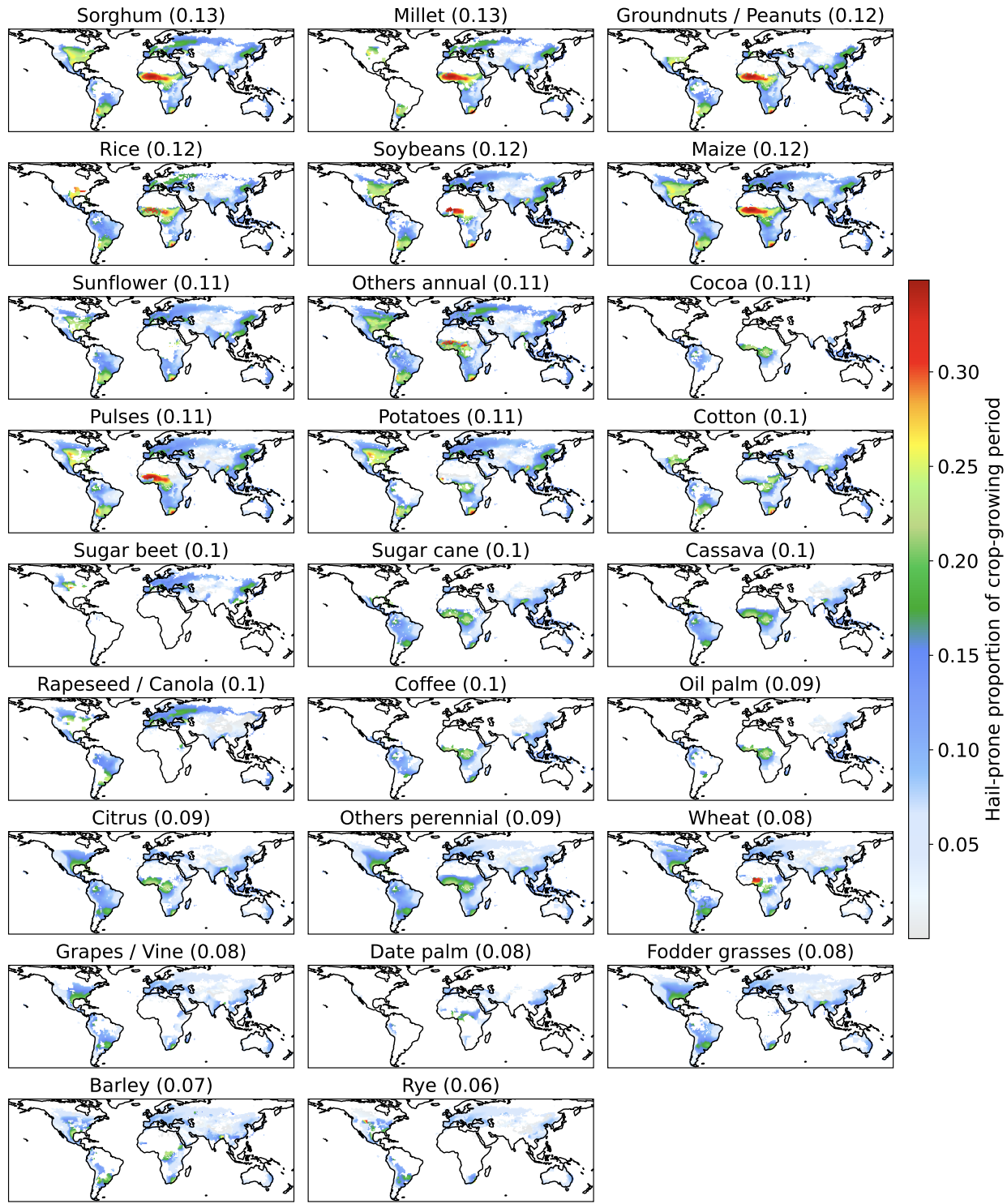
Supplementary Figure 4: **Differences in mean annual hail-prone days by model and proxy for 3 °C global warming.** Stippling shows regions for which the difference between epochs was statistically significant ($p < 0.05$ using Welch's t-test).



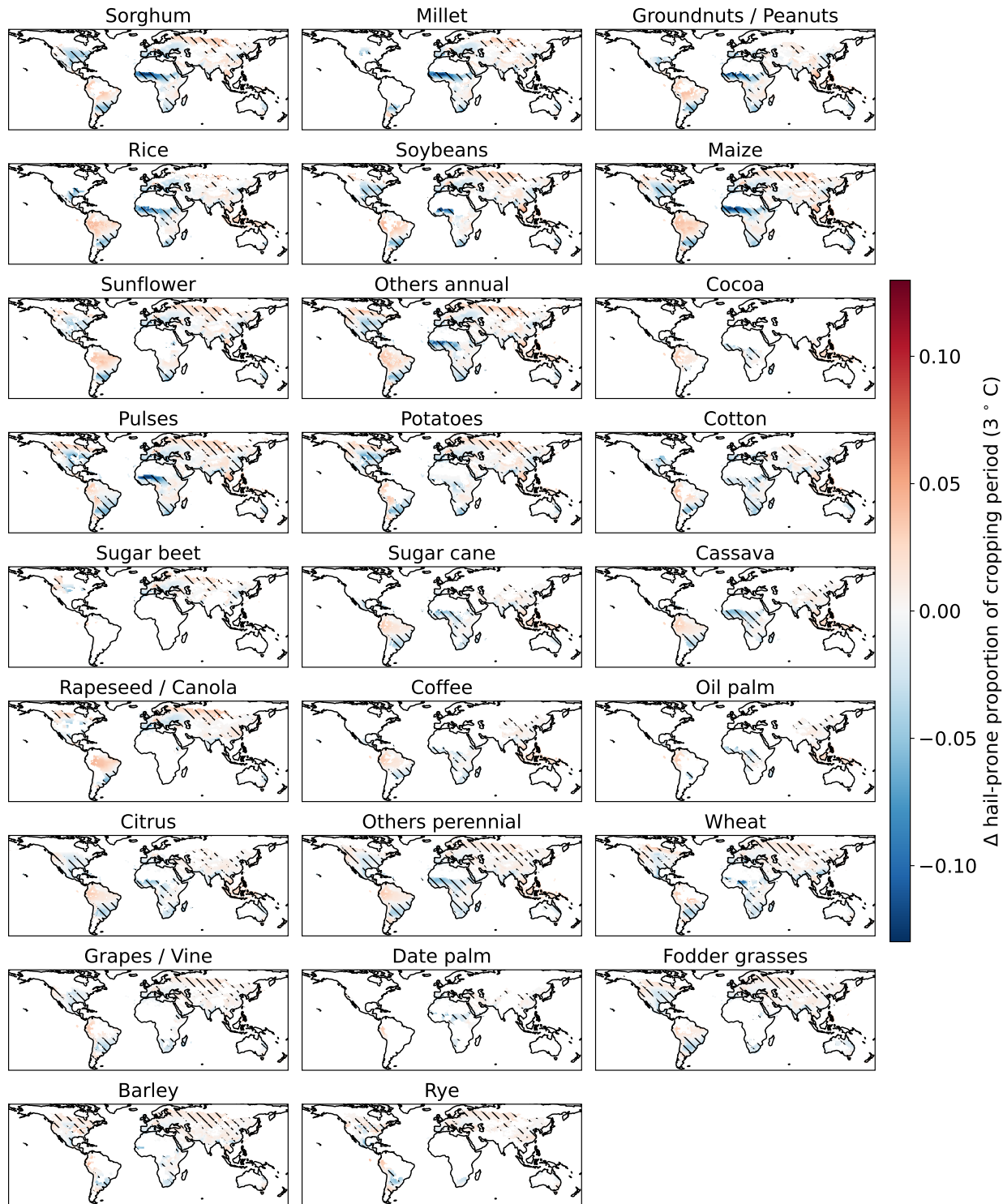
Supplementary Figure 5: **Multimodel mean differences in hail ingredients by epoch.** Ingredients shown are annual extreme (99th percentile) convective available potential energy (CAPE), annual extreme (99th percentile) 0-6 km bulk wind shear (S06), annual extreme (1st percentile) convective inhibition (CIN), and annual extreme (1st percentile) lifted index. Stippling shows regions in which at least 50% of the model/proxy combinations agreed with the sign of the mean difference and also showed significant differences in the mean ($p < 0.05$ on a t-test on two related samples).



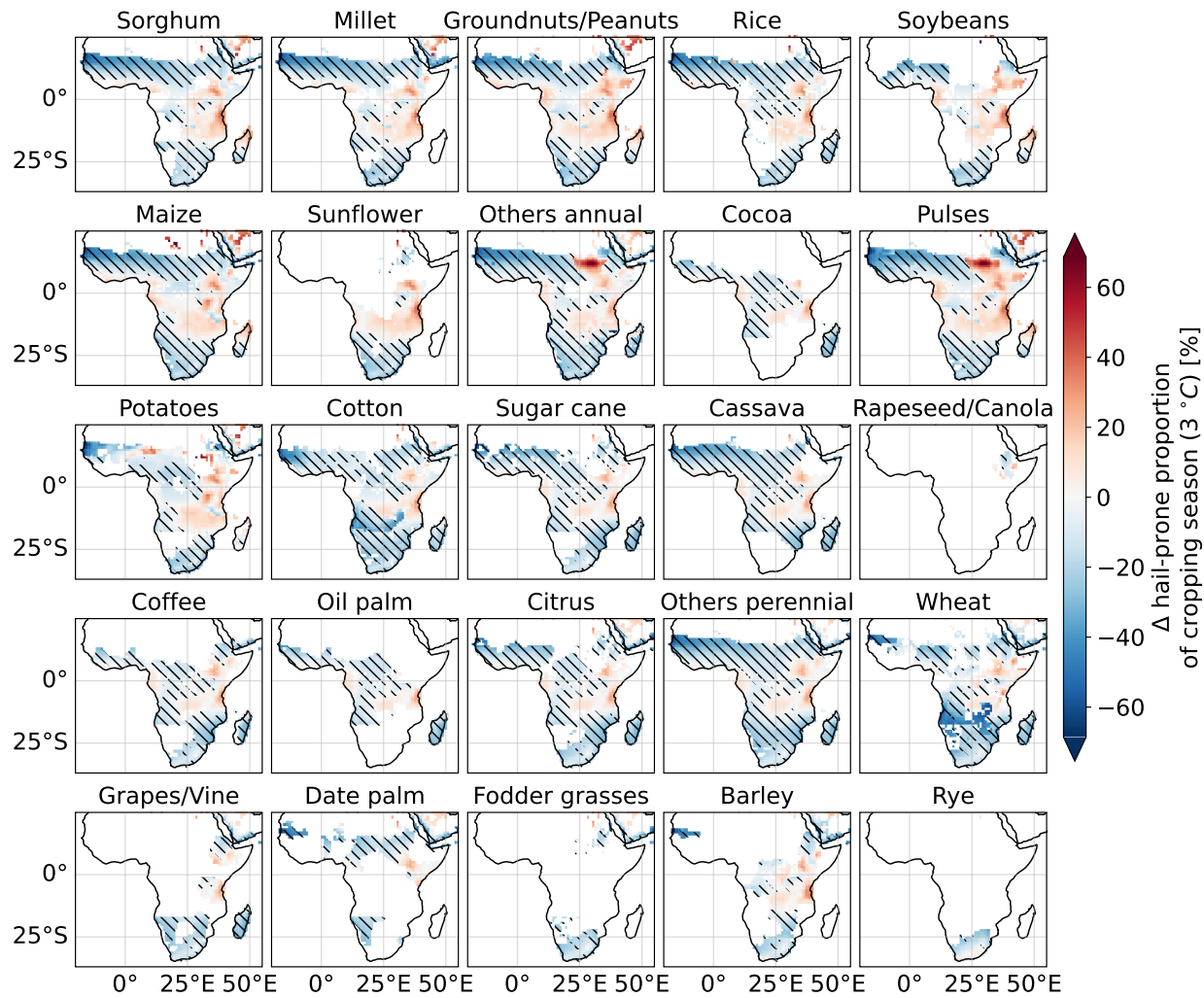
Supplementary Figure 6: As for Supplementary Figure 5 but for annual mean melting level height (MLH), annual mean temperature at 500 hPa (T_{500}), and annual mean lapse rate (LR). To increase contrast the colour scale for LR is truncated.



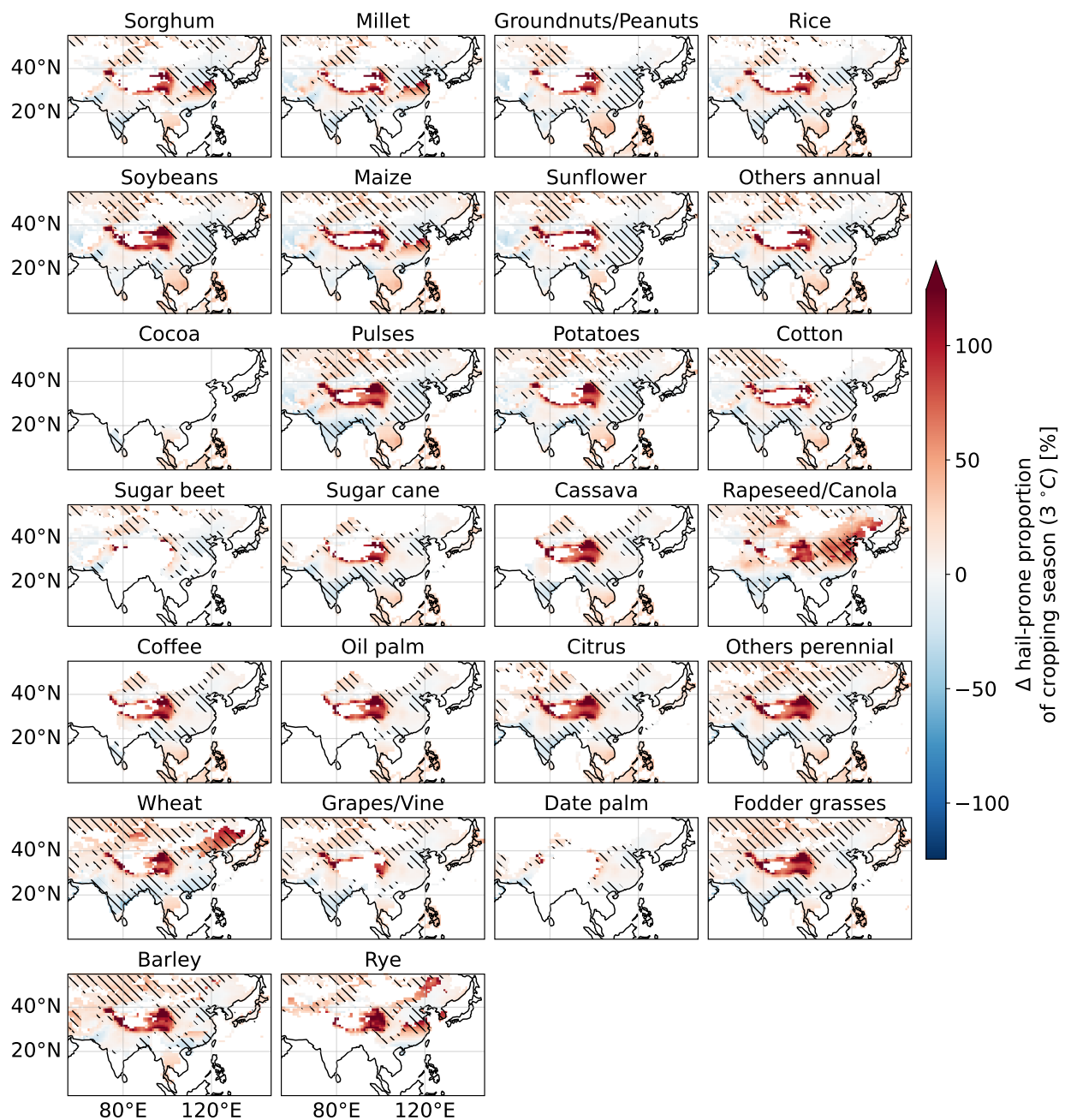
Supplementary Figure 7: **Multimodel, multi-proxy mean hail-prone proportions of cropping seasons for the historical period.** Brackets in titles show overall mean hail-prone proportion of cropping seasons by crop. Plots are subset to remove areas with no crop data.



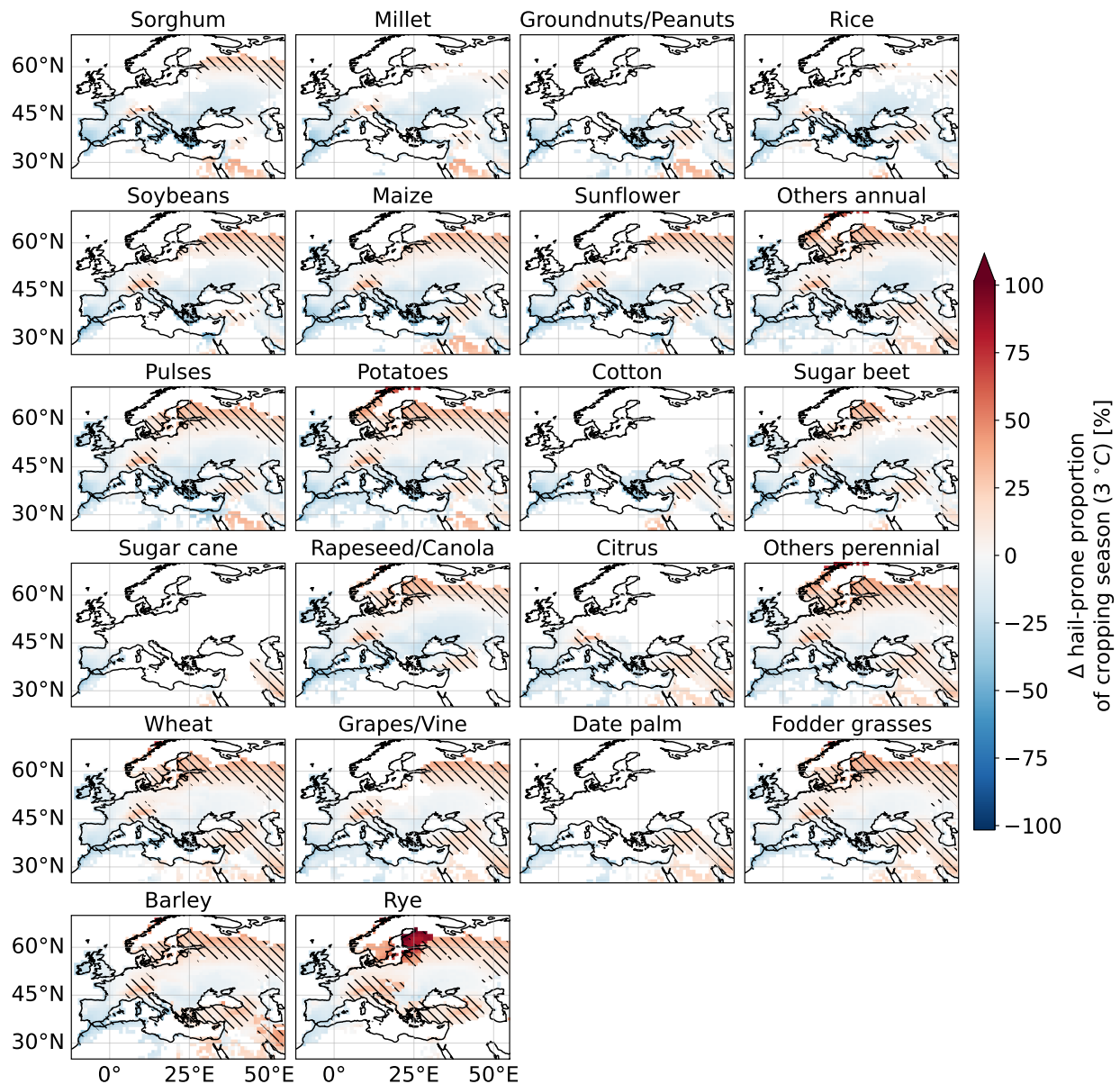
Supplementary Figure 8: **Multimodel, multi-proxy mean change in hail-prone proportions of cropping seasons for 3°C warming.** Stippling as for Supplementary Figure 5 and region subset as for Supplementary Figure 7.



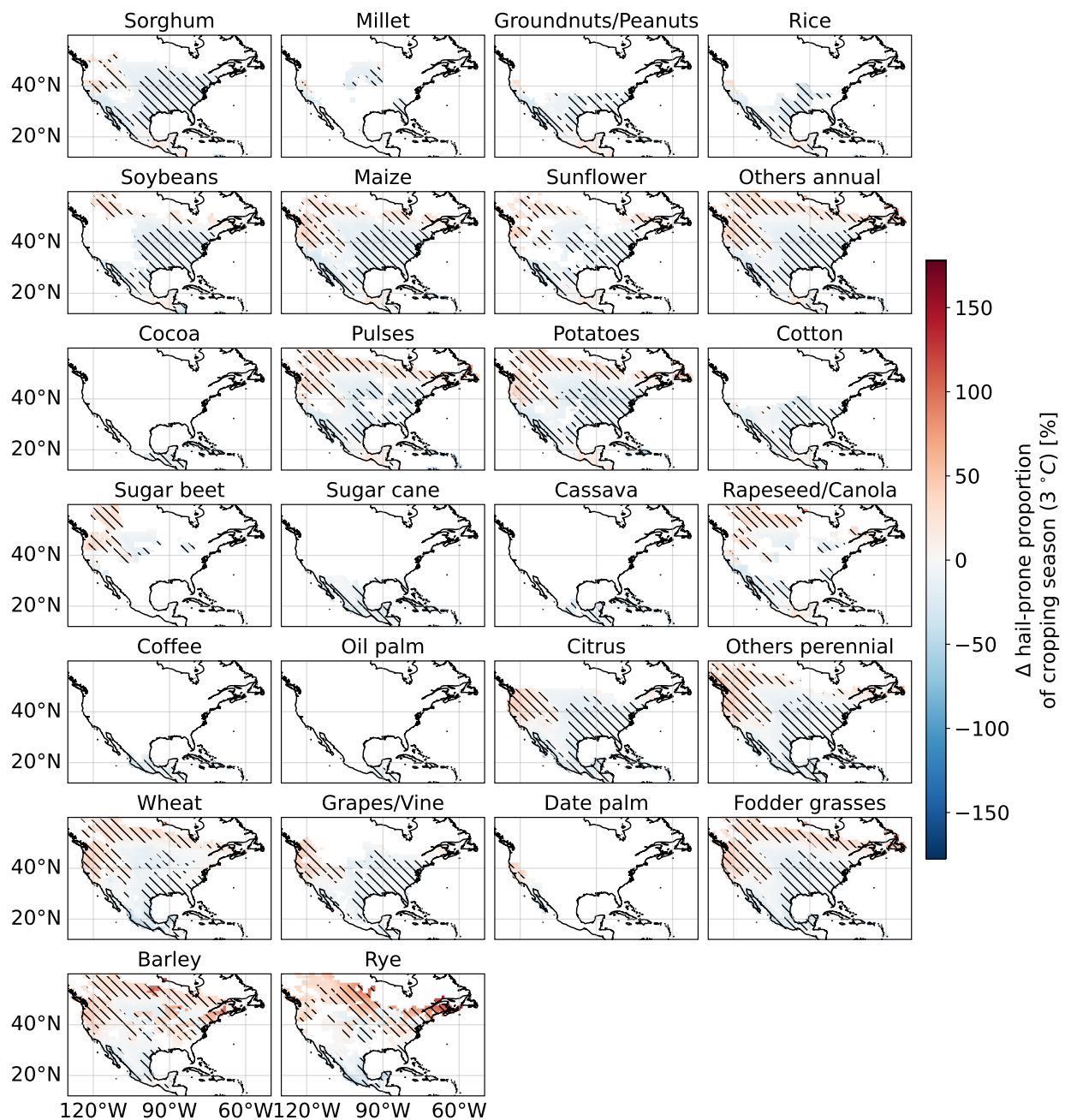
Supplementary Figure 9: Regional, relative changes in hail-prone proportion of cropping season. As for Supplementary Figure 8 but for Africa, and with changes shown as percentages of the historical hail-prone proportion of cropping season. Crops for which there were no significant changes recorded not shown. The colour bar is truncated to the range of stippled values and is non-linear with zero at the centre.



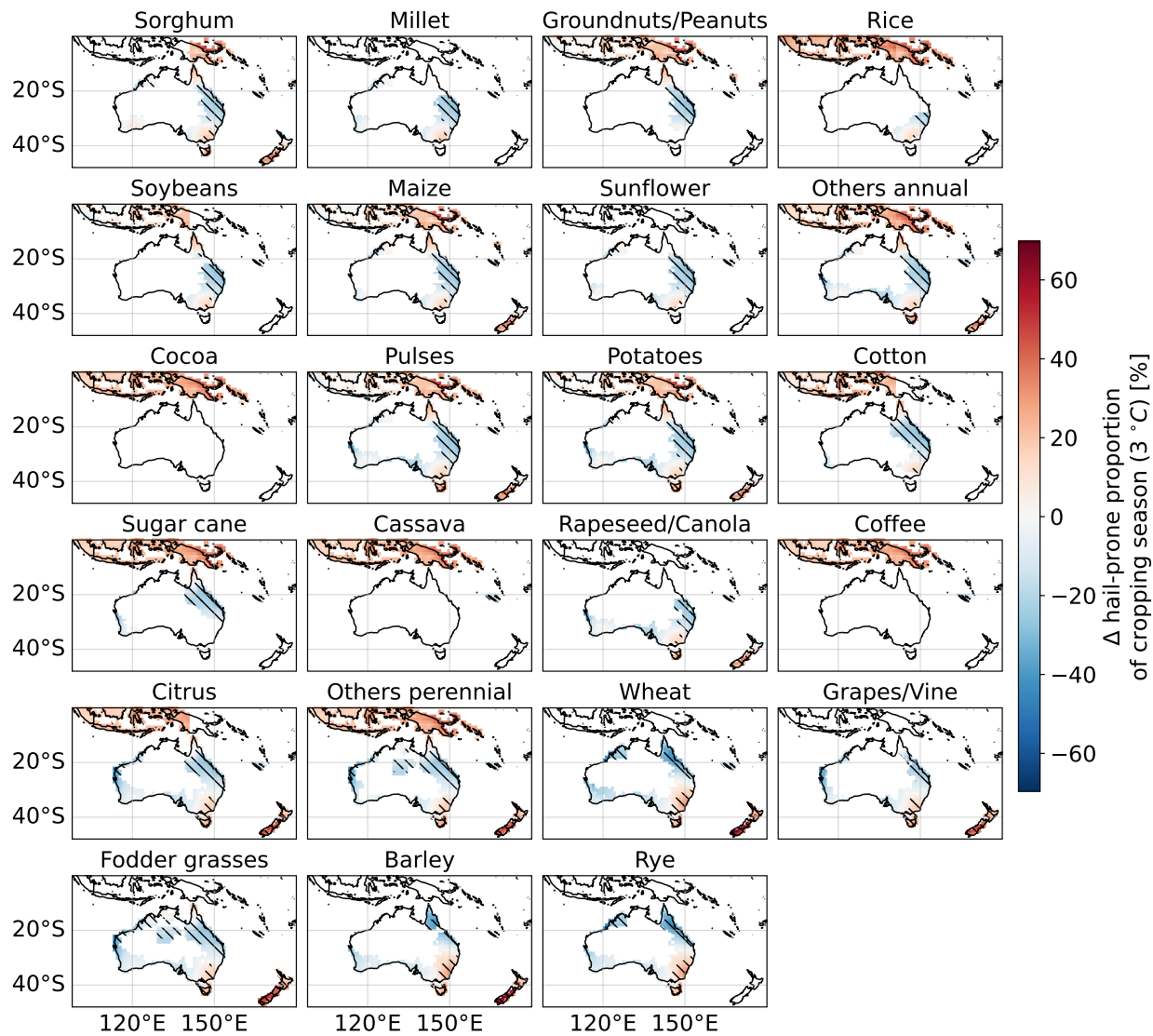
Supplementary Figure 10: As for Supplementary Figure 9 but for Asia.



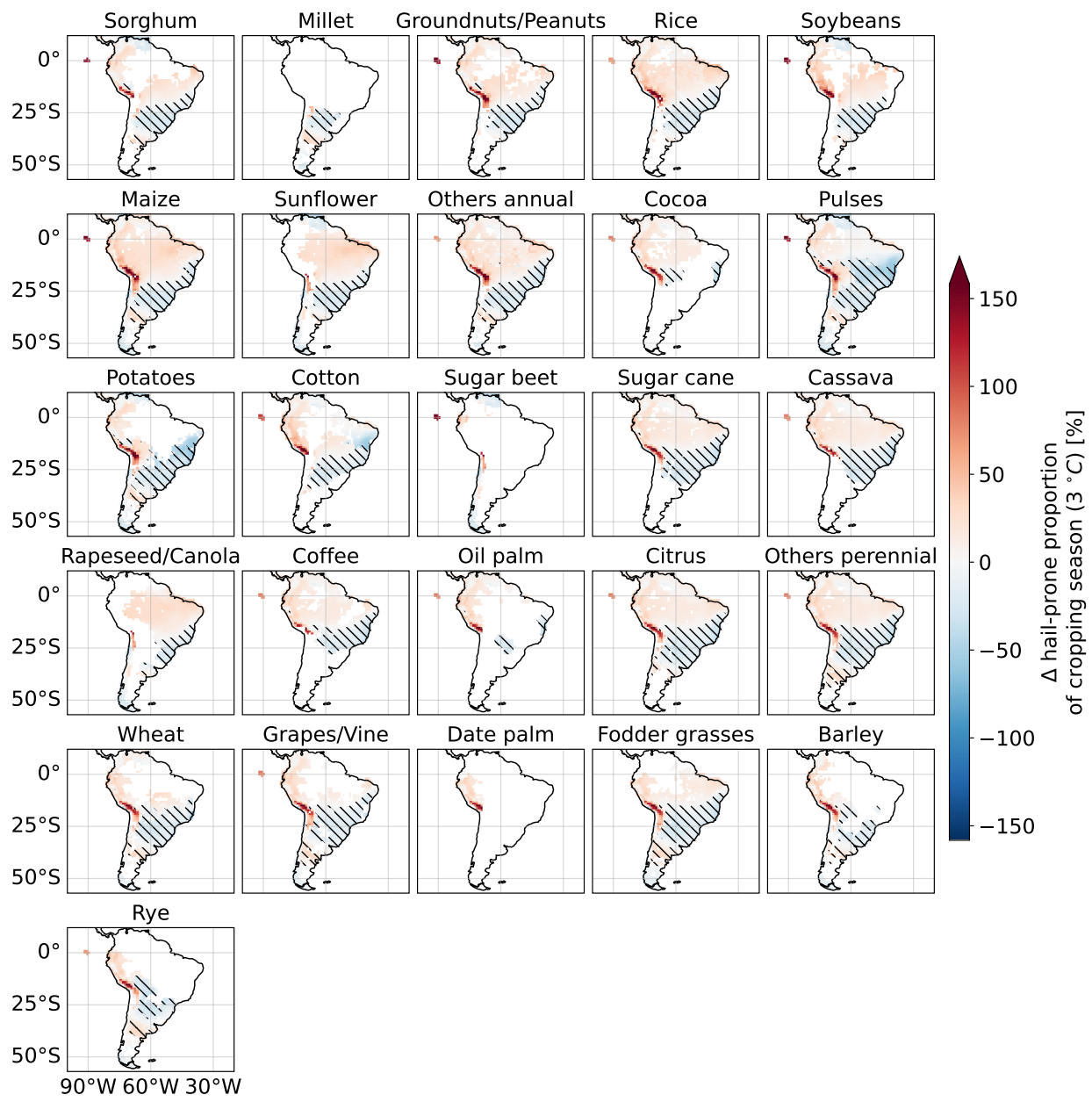
Supplementary Figure 11: As for Supplementary Figure 9 but for Europe.



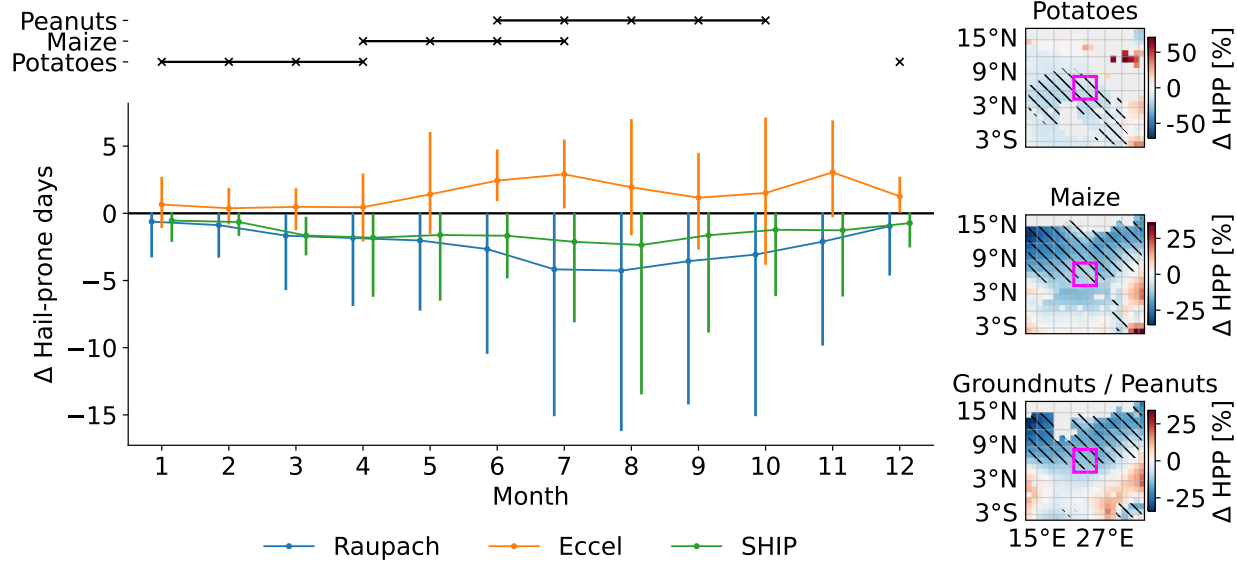
Supplementary Figure 12: As for Supplementary Figure 9 but for North America.



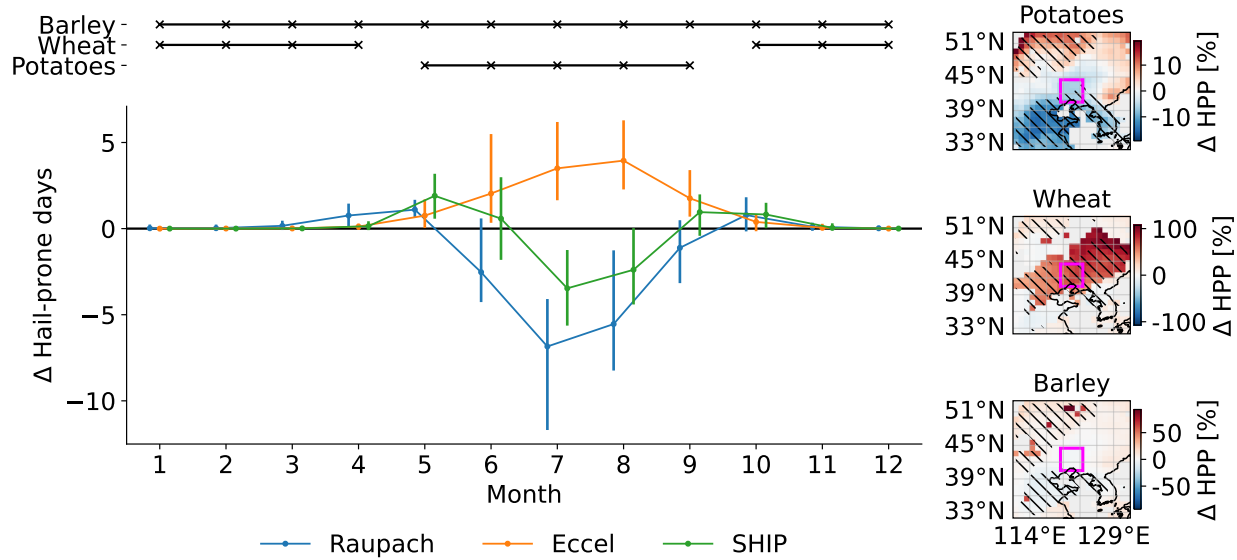
Supplementary Figure 13: As for Supplementary Figure 9 but for Oceania.



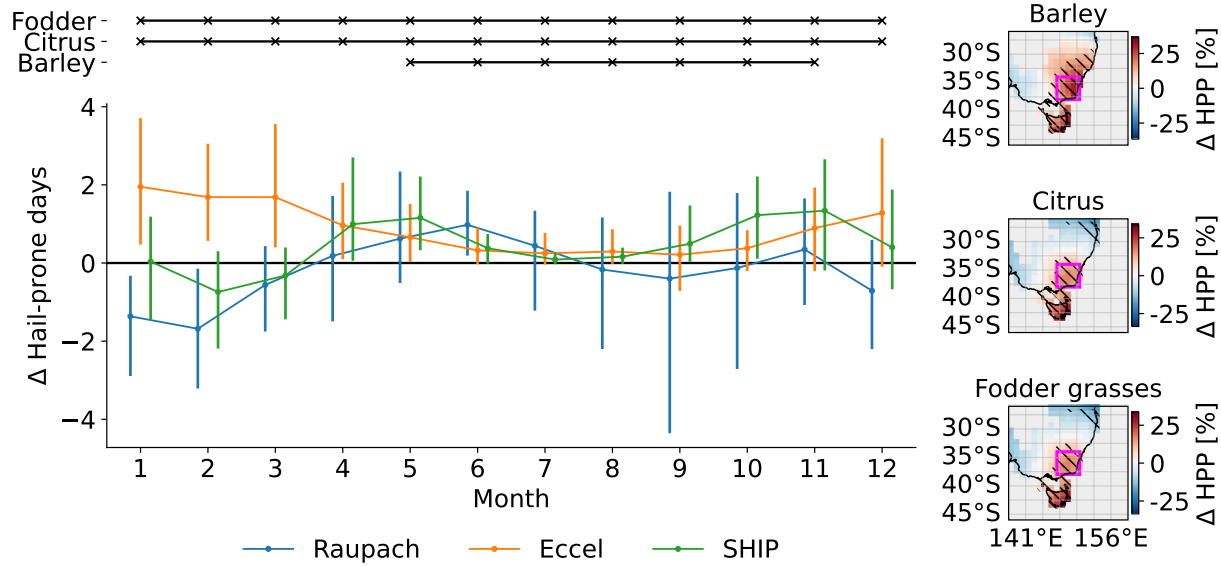
Supplementary Figure 14: As for Supplementary Figure 9 but for South America.



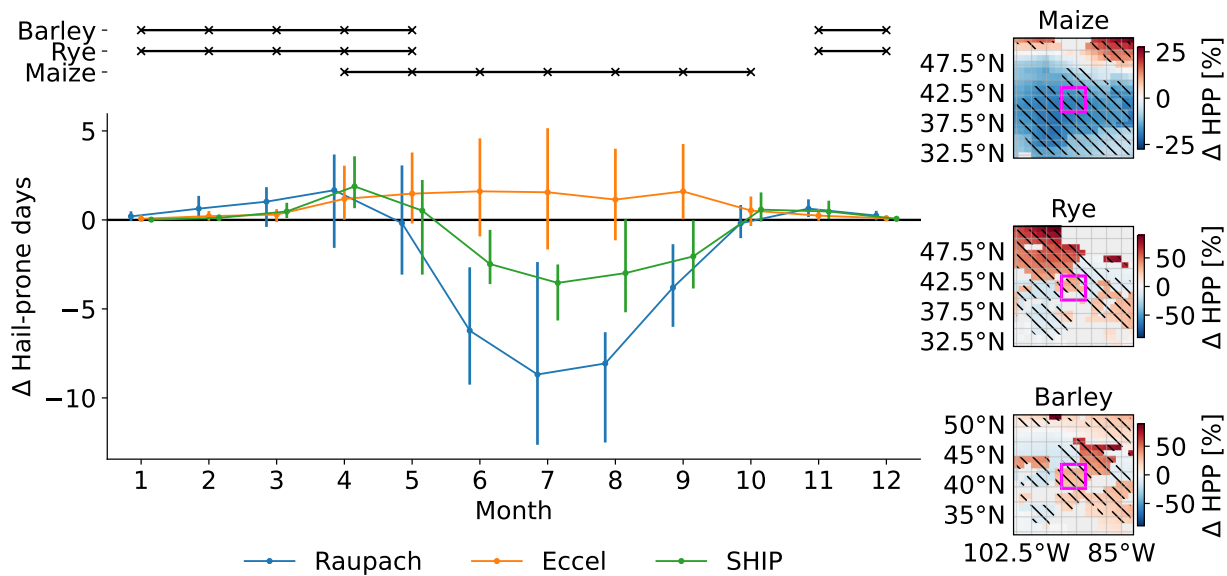
Supplementary Figure 15: Changes affecting crops at a selected location in Africa. The lines in the top inset plot indicate which months are considered cropping times for selected crops at the given location. The chosen location is at the centre of the fuchsia square in the inset maps. Inset maps show changes in hail-prone proportion of cropping season by crop. Lines in main plot show mean changes in hail-prone days per month over a $4 \times 4^{\circ}\text{C}$ region around the chosen location (shown as a fuchsia square in inset maps). Stippling in inset maps as for 5.



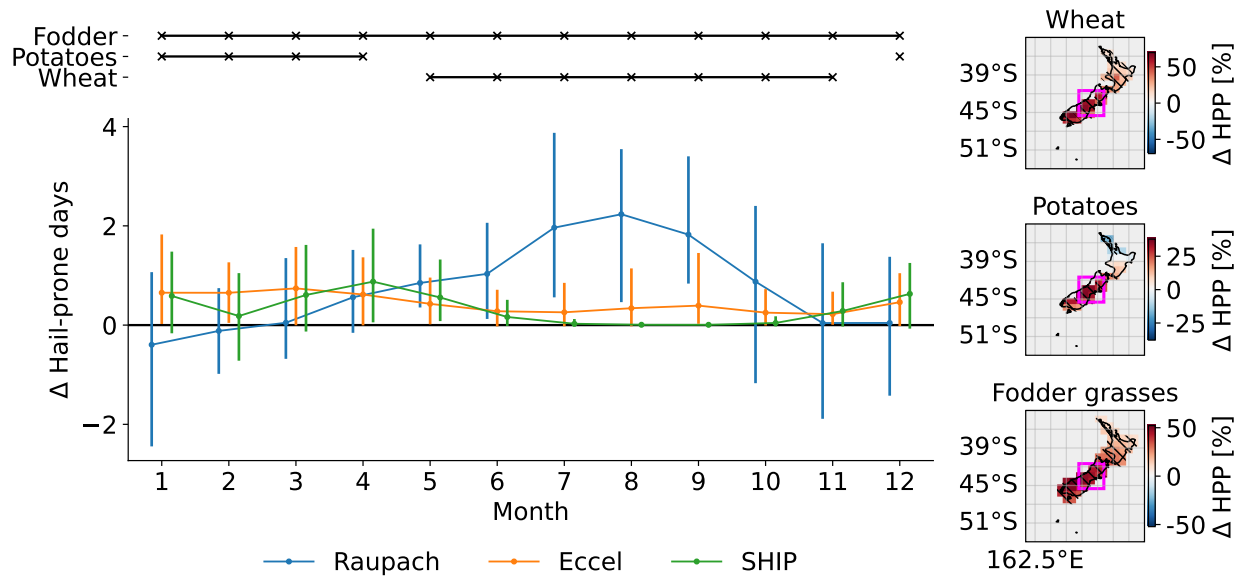
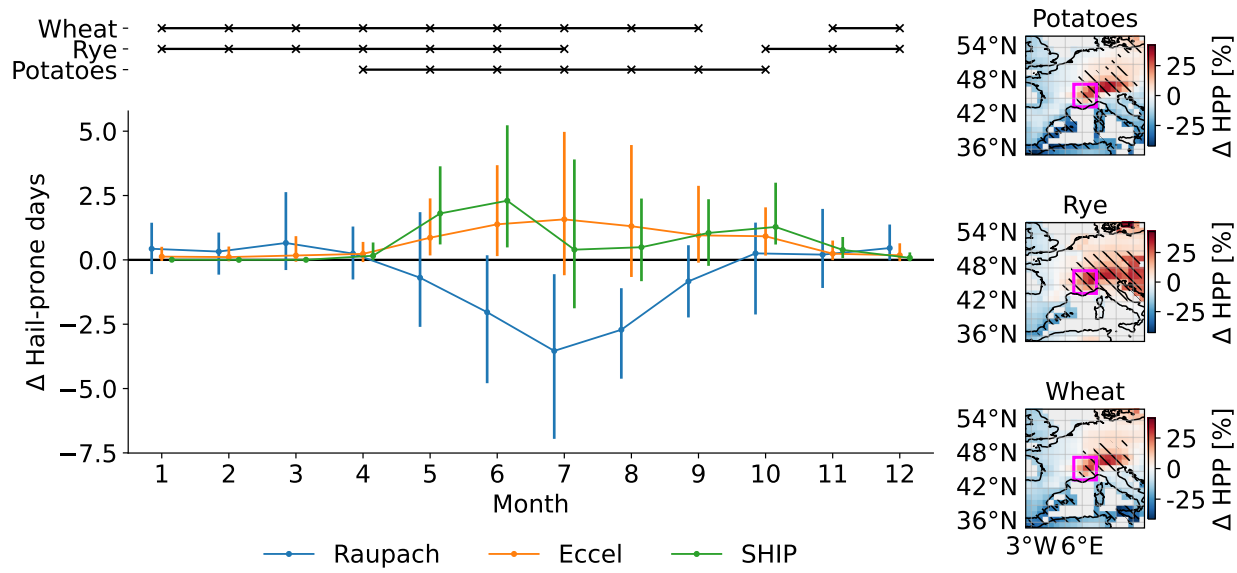
Supplementary Figure 16: As for Figure 15 but for Asia.



Supplementary Figure 17: As for Figure 15 but for Australia.



Supplementary Figure 18: As for Figure 15 but for the USA.



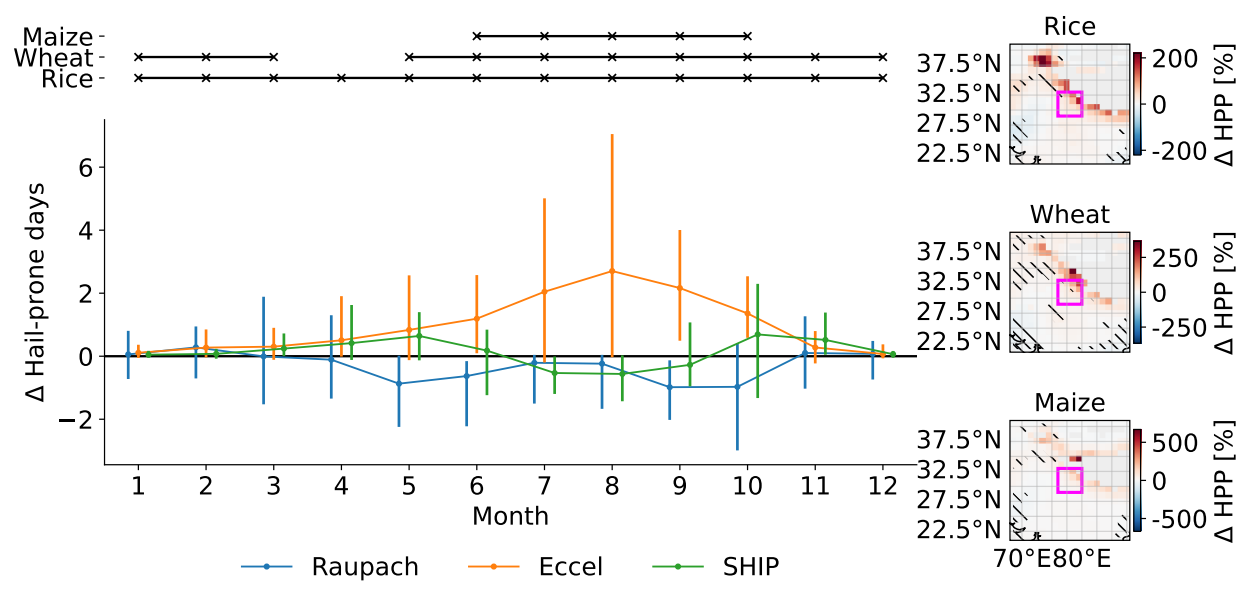
Supplementary Figure 20: As for Figure 15 but for New Zealand.

negative and the value of β becomes very small, and the proxy stops detecting high-CAPE, high-shear conditions.

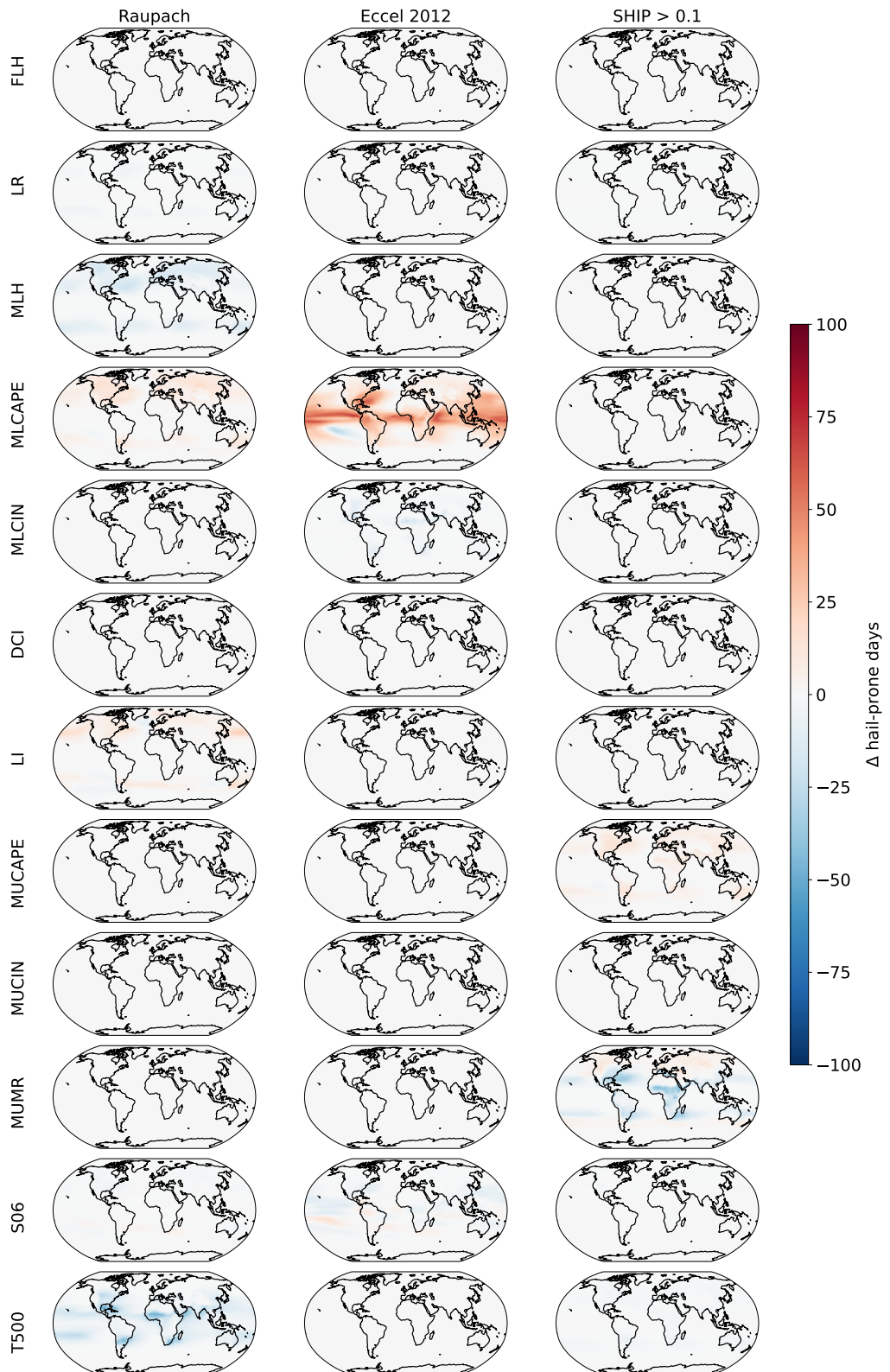
So that the proxy is more reliable in colder regions, in this work we have modified the proxy such that when the MLH is below 2000 m, the values of α and β for an MLH of 2000 m are used. With and without this modification the three original “extra conditions” defined in Raupach et al. [2023a] are similarly effective in removing false positives from the whole proxy training data set. We thus use these unmodified conditions. To assess the impact of this change we have tested on two datasets:

1. On the original training dataset from Raupach et al. [2023a], proxy performance metrics for the proxy with no extra conditions are similar between versions while the performance of the proxy with extra conditions is not affected by the change.
2. On the climatology data used in Raupach et al. [2023b] covering storm-prone hours of the day from 1979-2022 across all of Australia, the proxy changes affect the ocean areas in the south and southeast of the domain. However, over the whole map no location had more than 0.67% % of its values affected and over land no location had more than 0.35% of its values affected. The climatology and trends calculated using either version of the proxy are very similar.

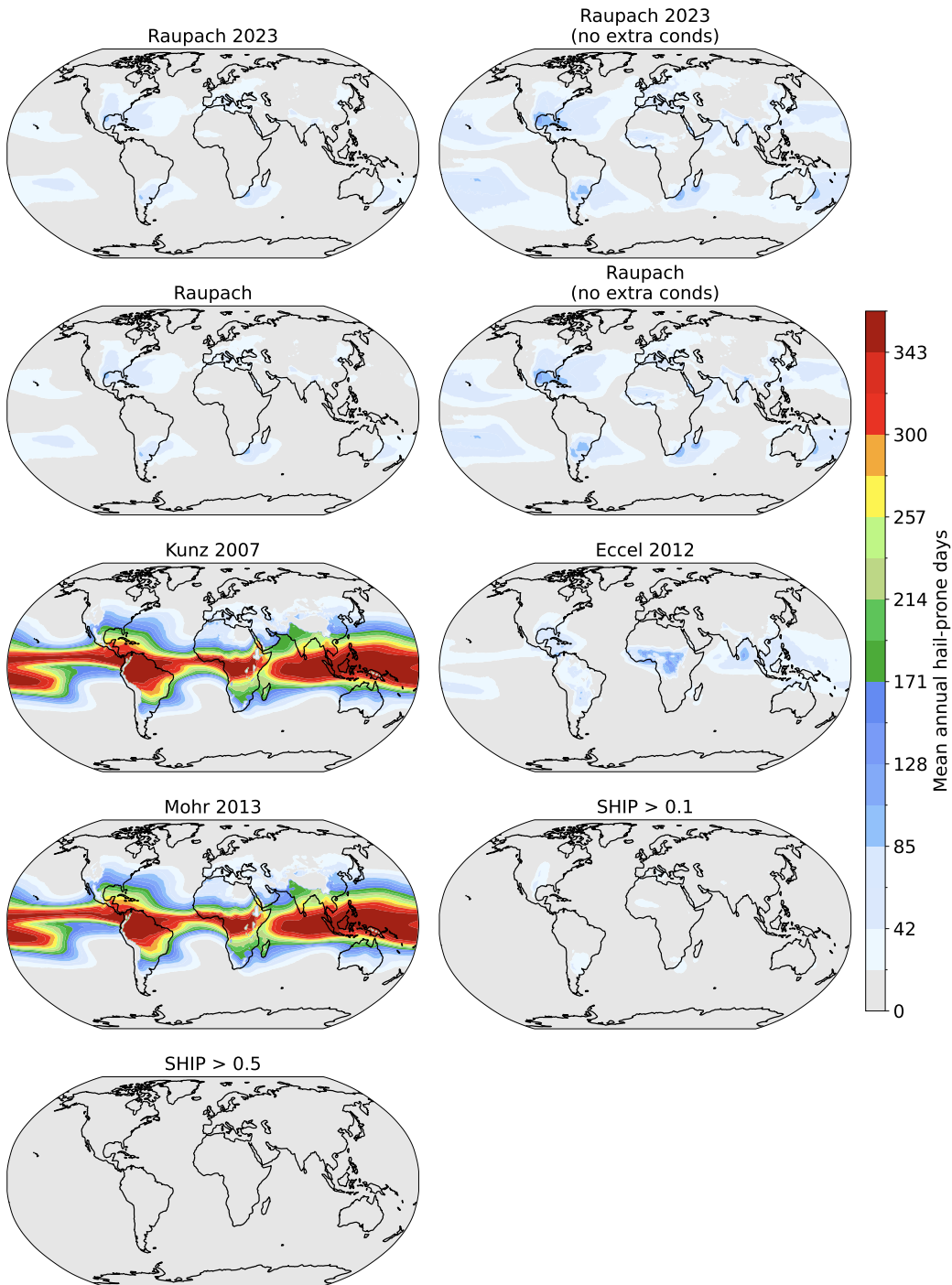
It is also notable that the projected changes in the Raupach proxy that we report in this work are not driven primarily by the “extra conditions”, as shown by Figure 25 here.



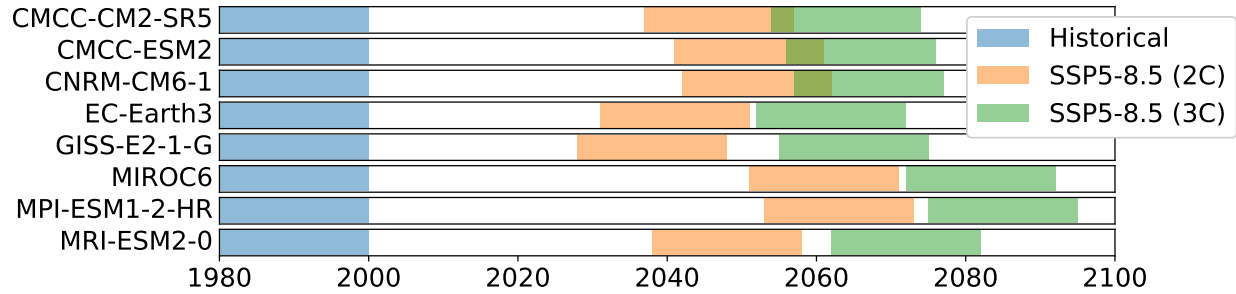
Supplementary Figure 21: As for Figure 15 but for India.



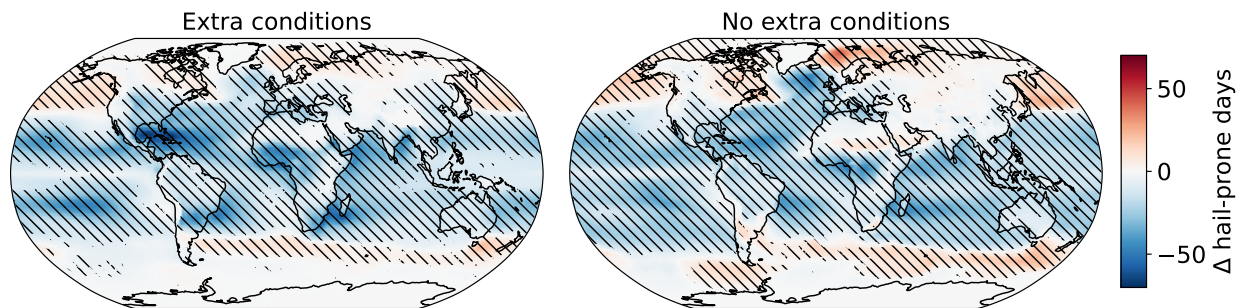
Supplementary Figure 22: Drivers of changes across models. Rows show de-biased ingredients: freezing level height (FLH), lapse rate (LR), melting level height (MLH), mixed-layer CAPE (MLCAPE), mixed-layer CIN (MLCIN), deep convective index (DCI), lifted index (LI), most-unstable CAPE (MUCAPE), most-unstable CIN (MUCIN), most-unstable mixing ratio (MUMR), 0-6 km bulk shear (S06), and temperature at 500 hPa (T500).



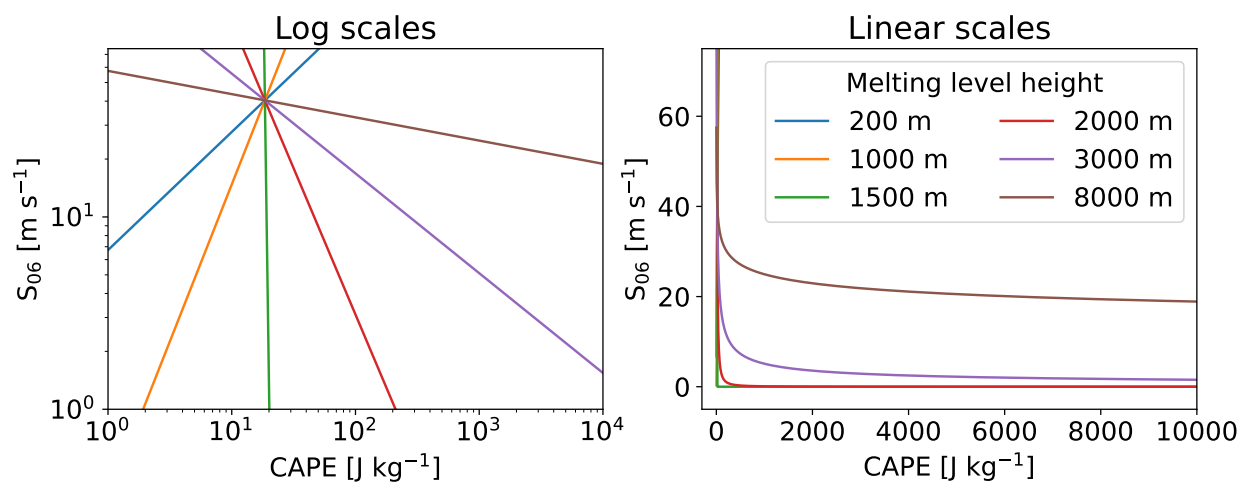
Supplementary Figure 23: Mean annual hail-prone days for ERA5 reanalysis (1980-1999) for all applied hail proxies. The proxies of Kunz [2007] and Mohr and Kunz [2013] produced unrealistically many hail-prone days in tropical regions for which they were not trained [Raupach et al., 2023a], and a threshold of 0.5 on SHIP, as has been used in other studies for severe hail [Prein and Holland, 2018], was found to produce too few hail-prone days in comparison with the other proxies designed for hail of any size.



Supplementary Figure 24: CMIP6 models and per-degree-framework date ranges. The reference period from historical simulations is shown in blue, while periods with 2 and 3 °C warming over the reference period, in SSP5-8.5 simulations, are in orange and green respectively.



Supplementary Figure 25: Effect of extra conditions on Raupach proxy for 3 °C warming. Changes shown are multi-model mean changes in annual hail-prone days. On left, the updated Raupach proxy with extra conditions designed to remove false positives applied as used in the rest of this study and explained in Section 2; on right, changes in the updated Raupach proxy without extra conditions applied.



Supplementary Figure 26: **Original proxy for various values of melting level height (MLH).** CAPE stands for convective available potential energy. S_{06} is 0-6 km bulk vertical wind shear. The same discriminator lines are shown on logarithmic and linear scales.

Supplementary References

- M. Kunz. The skill of convective parameters and indices to predict isolated and severe thunderstorms. *Nat. Hazards Earth Sys.*, 7(2):327–342, 2007. ISSN 1561-8633. doi: 10.5194/nhess-7-327-2007.
- S. Mohr and M. Kunz. Recent trends and variabilities of convective parameters relevant for hail events in Germany and Europe. *Atmos. Res.*, 123:211–228, 2013. ISSN 0169-8095. doi: 10.1016/j.atmosres.2012.05.016.
- Timothy H. Raupach, Joshua Soderholm, Alain Protat, and Steven C. Sherwood. An improved instability–shear hail proxy for australia. *Mon. Weather Rev.*, 151(2):545–567, 2023a. doi: 10.1175/MWR-D-22-0127.1.
- Andreas F. Prein and Greg J. Holland. Global estimates of damaging hail hazard. *Weather Clim. Extremes*, 22:10–23, 2018. ISSN 2212-0947. doi: 10.1016/j.wace.2018.10.004.
- Timothy H. Raupach, Joshua S. Soderholm, Robert A. Warren, and Steven C. Sherwood. Changes in hail hazard across australia: 1979–2021. *npj Clim. Atmos. Sci.*, 6(1):143, 2023b. ISSN 2397-3722. doi: 10.1038/s41612-023-00454-8.